Numerical Simulation of the In-Situ Upgrading of Oil Shale

Y. Fan, SPE, **L.J. Durlofsky,** SPE, and **H.A. Tchelepi,** SPE, Stanford University

Summary

Oil shale is a highly abundant energy resource, though commercial production has yet to be realized. Thermal in-situ upgrading processes for producing hydrocarbons from oil shale have gained attention recently, however, in part because of promising results reported by Shell using its in-situ conversion process (Crawford et al. 2008). This and similar processes entail heating the oil shale to approximately 700°F (371°C), where the kerogen in the shale decomposes through a series of chemical reactions into liquid and gas products. In this paper, we present a detailed numerical formulation of the in-situ upgrading process. Our model, which can be characterized as a thermal/compositional, chemical reaction, and flow formulation, is implemented into Stanford's General Purpose Research Simulator (GPRS). The formulation includes strongly temperature-dependent kinetic reactions, fully compositional flow and transport, and a model for the introduction of heat into the formation through downhole heaters. We present detailed simulation results for representative systems. The model and heating patterns are based on information in Shell publications; chemical-reaction and thermodynamic data are from previously reported pyrolysis experiments. After a relatively modest degree of parameter adjustment (with parameters restricted to physically realistic ranges), our results for oil and gas production are in reasonable agreement with available field data. We also investigate various sensitivities and show how production is affected by heater temperature and location. The ability to model these effects will be essential for the eventual design and optimization of in-situ upgrading operations.

Introduction

Oil shales are organic-rich sedimentary rocks that contain significant amounts of kerogen and generate oil upon pyrolysis or retorting (Peters et al. 2005). Oil-shale deposits are found in many parts of the world, and the kerogen in oil shales is recognized as one of the most abundant energy resources. A conservative estimate suggests that the total worldwide oil-shale resources are equivalent to approximately 3×10^{12} bbl of oil (Dyni 2006). The Green River formation in the western USA is the largest known oil-shale deposit in the world, containing approximately 1.5×10^{12} bbl of shale oil (Dyni 2006). Although technologies for oil-shale processing have been investigated actively in past decades (Biglarbigi et al. 2007), there has been renewed interest in recent years because of both high oil prices and the promising field-test results of Shell's in-situ conversion process (Crawford et al. 2008). Assuming oil-shale production technologies are able to address issues related to water use and carbon dioxide emissions successfully (Brandt 2008), it is quite possible that oil shales may contribute to the future oil supply.

Kerogen in oil shales is believed to originate from the same types of organic matter that generated existing oil and gas accumulations. In the case of the oil shales, however, the natural maturation process, which would eventually lead to oil and gas, is at a very early stage and may still require millions of years. This process can be accelerated through either surface retorting or in-situ upgrading. Surface retorting requires that the oil shale be mined, followed by surface pyrolysis and further processing. This method is suitable only for shallow formations that can be mined economically. In-situ upgrading, by contrast, entails heating the oil shale in-situ using downhole heaters. Once the temperature reaches the appropriate window, chemical reactions occur and high-quality products (with chemical composition resembling that of light oil) can be produced. Because the in-situ upgrading process does not require mining, it is applicable for deeper oil-shale deposits. Biglarbigi et al. (2007) estimated that, for a plant of 100,000-B/D capacity to operate economically, the oil price must be at least USD 35 per barrel of oil.

There are many technical, environmental, and economic challenges associated with the in-situ upgrading and production of oil shales. In order to understand these issues better, and to design optimal production processes that minimize environmental impact, it is essential that we develop an accurate and efficient modeling capability. This represents a challenge, however, because the model must, at a minimum, entail a fully compositional formulation that includes thermal effects and chemical reactions. Additional capabilities, such as thermal-well models and geomechanical models, may also be required.

Our goal in this work is to develop a thermal/chemical formulation within the context of a general compositional framework and to apply it for the simulation of the in-situ upgrading process. To accomplish this, we implement chemical-reaction-modeling capabilities into GPRS (Cao 2002; Jiang 2008). The chemical-kinetics model is based on reaction-rate laws expressed in terms of the concentrations of each component in each phase. Additionally, we introduce a mineral phase into the kinetics module to simulate kerogen decomposition. The kinetics module is fully coupled with the mass and energy balances and with the system thermodynamics. Phase equilibrium is modeled using the Peng-Robinson equation of state (EOS). The resulting formulation is also applicable for simulating the upgrading of other resources, such as tar sands.

A number of previous studies are relevant to this work. A single-block kinetic model for oil-shale pyrolysis was developed by Burnham and Braun (1984). This model provides predictions for oil generation, given the pressure/temperature history. In later work, Braun and Burnham (1990) presented a general chemical-reaction model for oil and gas generation and compared model results to pyrolysis data. This model was a general chemical-kinetics formulation that included 83 species and 100 reactions and was coupled with the Redlich-Kwong-Soave EOS. Later, Burnham and Braun (1993) developed a simpler model consisting of 13 chemical species and 10 chemical reactions to simulate the oil generation and expulsion from petroleum source rocks. This model was applied mainly to the oil-generation process at geologic conditions. To our knowledge, it has not been implemented into a flow simulator for modeling coupled in-situ upgrading and flow processes.

Shell has applied the commercial thermal reservoir simulator STARS to model its in-situ upgrading field tests (Vinegar 2006). STARS is a generalized thermal/compositional simulator coupled with chemical kinetics (STARS 2008). The phase-equilibrium calculations in STARS are based on *K*-values and, thus, require a significant amount of experimental data if the number of species is large. Our formulation, by contrast, uses an EOS to calculate phase behavior. By ensuring full consistency between the *K*-values and the EOS description, it is possible, in principle, to compare the results from STARS against our model. However, because much of Shell's work on in-situ upgrading is proprietary, detailed descriptions of its use of STARS for this problem are not available. Thus, we have not attempted to compare our simulation predictions with Shell's.

This paper (SPE 118958) was accepted for presentation at the SPE Reservoir Simulation Symposium, The Woodlands, Texas, USA, 2–4 February 2009, and revised for publication. Original manuscript received for review 3 November 2008. Revised manuscript received for review 22 September 2009. Paper peer approved 30 September 2009.

We apply our in-situ upgrading model to simulate the Mahogany Demonstration Project-South (MDP-S), conducted by Shell (Fowler and Vinegar 2009). This field test entails the use of 16 downhole electrical heaters placed in a pattern along with three production wells. Data for the kerogen and the kerogen decomposition products are taken from measurements of the pyrolysis of Green River oil shales reported by Braun and Burnham (1990). With only minimal tuning of input parameters, our simulations provide results for oil and gas production in reasonably close agreement with the MDP-S, which provides a degree of validation for our simulation model. We then perform a sensitivity analysis to study the effect of heater temperature, pattern type, and pattern spacing on oil and gas production. Such assessments will be essential for the optimization of this process in practice.

In-Situ Upgrading Model

The simulation of in-situ upgrading involves (primarily) the modeling of chemical kinetics, phase equilibrium between the gas and liquid phases, mass transport, and heat conduction. The chemical kinetics is highly temperature-dependent and, thus, is strongly coupled with both the mass- and energy-balance equations. Our simulator already can model general thermal/compositional problems, so the main new element, which we discuss in detail here, is the incorporation of chemical kinetics. This capability is one component of a new unified simulation framework for chemical-reaction modeling that handles both kinetic and equilibrium reactions.

The actual in-situ upgrading process is very complicated, and there are some physical effects not incorporated in our model. These include geomechanical effects and evolution of porosity and permeability (which occur as the kerogen decomposes). Thus, our model applies "average" or "effective" values for porosity and permeability, though it may be useful to develop more-sophisticated treatments for these effects in future work. We now describe the specific treatments included in the in-situ upgrading model.

Mass- and Energy-Balance Equations. The mass-balance equation for chemical/compositional simulation can be expressed for each fluid component i as follows [adapted from Cao (2002) and Lake (1989)]:

$$F_i = \frac{\partial}{\partial t}\left[\phi\sum_j\left(S_j\rho_j X_{ij}\right)\right] - \sum_j\sum_k\left(\nu'_{ij,k}-\nu_{ij,k}\right)r_k + \nabla\cdot\sum_j\left(\rho_j X_{ij}\mathbf{u}_j\right) + \sum_j \rho_j X_{ij} q_j^W = 0, \quad \ldots\ldots\ldots\ldots\ldots\ldots (1)$$

where F_i represents the residual of the mass-balance equation for component i, ϕ is the porosity, S_j is the saturation of phase j, X_{ij} is the mole fraction of component i in phase j, k is the kinetic reaction index, $\nu'_{ij,k}$ and $\nu_{ij,k}$ are stoichiometric coefficients for component i as product and reactant, r_k is the rate of reaction k, $\mathbf{u}_j$ is the Darcy velocity for phase j, ρ_j is the density of phase j, and q_j^W is the well rate of phase j. The Darcy velocity is given by

$$\mathbf{u}_j = -\mathbf{K}\frac{k_{rj}}{\mu_j}\left(\nabla p_j - \gamma_j \nabla D\right), \quad \ldots\ldots\ldots\ldots\ldots\ldots\ldots\ldots (2)$$

where $\mathbf{K}$ is the permeability tensor, k_{rj} is the relative permeability for phase j, μ_j is the viscosity of phase j, p_j is the pressure of phase j, $\gamma_j = \rho_j g/g_c$ (g is gravitational acceleration, and g_c converts from lbm to lbf), and D is depth.

The simulator can account for any number of solid components. Each solid component is described by one additional mass-balance equation [adapted from Lake (1989)]:

$$F_s = \frac{\partial C_s}{\partial t} - \sum_k\left(\nu'_{s,k}-\nu_{s,k}\right)r_k = 0, \quad \ldots\ldots\ldots\ldots\ldots\ldots (3)$$

where C_s is the molar concentration of solid s and $\nu'_{s,k}$ and $\nu_{s,k}$ are the stoichiometric coefficients of solid s in reaction k as product and reactant. When modeling in-situ upgrading processes, kerogens are treated as solid components governed by Eq. 3. Some oil-shale formations may contain various types of kerogens and, thus, require more than one solid mass-balance equation. The simulator can treat chemical reactions involving multiple solid components; though, for simplicity, only one type of kerogen is modeled in this work.

In order to account for the effects of thermal convection and heat conduction, an energy-balance equation for the system is required. The energy equation is given by [adapted from Lake (1989)]:

$$F_e = \frac{\partial}{\partial t}\left[\phi\left(\sum_j U_j\rho_j S_j\right) + (1-\phi)U_R\right] - \nabla\cdot\left(\sum_j H_j\rho_j\mathbf{u}_j\right) - \nabla\cdot(\kappa\nabla T) + \sum_j H_j\rho_j q_j^W + q^H = 0, \quad \ldots\ldots\ldots\ldots\ldots\ldots (4)$$

where U_j is the internal energy for phase j, U_R is the internal energy of the rock, $H_j = \sum_i X_{ij}H_i$ is the enthalpy of phase j, κ is the thermal conductivity of oil shale, and q^H is the rate of energy input from downhole heaters. We do not include heat-of-reaction terms in Eq. 4 because these effects are very small relative to heat input (Pan et al. 1984).

Phase Equilibrium and Properties. Upon heating, the kerogen decomposes to a multicomponent mixture. The mixture may contain noncondensable gases, hydrocarbons, water, and prechar. These components constitute at least four phases—a gas phase, an oil phase, a water phase, and a solid prechar phase. In general, each phase is a mixture of multiple components, with the partitioning of the components between the phases described by thermodynamic relationships.

In this work, we assume that the prechar phase is created and retained in the solid phase. Therefore, the prechar phase is assumed not to occupy the pore space. Under this assumption, we do not need to consider the prechar in the transport equations. Although the water and oil phases are immiscible, water vapor and hydrocarbon gases are miscible. These assumptions together require that three-phase flash calculations be performed. Such flash calculations require significant computational effort and will affect the performance of our simulator. In typical in-situ upgrading processes, however, the reactions of interest occur mostly above the boiling point of water. Also, if possible, water in the formation is produced before heating to avoid expending energy to heat and vaporize water. For these reasons, only gas/oil phase equilibrium is considered here. The gas phase may contain noncondensable gases and hydrocarbons, while the oil phase may contain condensable gases and hydrocarbons. This treatment is reasonable when the amount of water produced during the in-situ upgrading process is small. If this is not the case, then the water phase (and three-phase calculations) must be included in the model.

Thermodynamic equilibrium requires the equality of component fugacities in the gas and oil phases

$$f_i^o - f_i^g = 0, \quad \ldots\ldots\ldots\ldots\ldots\ldots\ldots\ldots\ldots\ldots\ldots\ldots (5)$$

where f_i^o and f_i^g are the fugacities of component i in the oil and gas phases, respectively. The phase densities are calculated by the Peng-Robinson EOS. The viscosity of the gas phase is modeled using a standard mixing rule for EOS calculations from Jossi et al. (1962). The viscosity of the oil phase is determined using the representation given by Miadonye et al. (1994):

$$\log_{10}\mu_o(T) = b\left(1+\frac{T-30}{303.15}\right)^{-s} + c, \quad \ldots\ldots\ldots\ldots\ldots (6)$$

where b, c, and s are parameters evaluated from measurements for the oil under study. Note that T in Eq. 6 is temperature in °C. In the simulations presented in this paper, we use $b = 4.1228$, $s = 3.5640$, and $c = -3.002$.

Kinetic Reactions. Chemical reactions can be divided into two groups, equilibrium reactions and kinetic reactions. Equilibrium reactions are reversible and proceed quickly relative to the timestep of the simulation; therefore, these reactions can be assumed to remain in equilibrium. Kinetic reactions, by contrast, do not necessarily remain in equilibrium over the timestep of interest, so reaction kinetics must be considered in this case. Treatments for both equilibrium and kinetic reactions have recently been incorporated into the simulator. Here, we describe our implementation only for kinetic reactions because these are the reactions involved in the in-situ upgrading process.

In Eq. 1, the reaction rate r_k is generally expressed in terms of species concentration. Considering reactions in which reactants can be either fluid components or solid components, and assuming that all reactions follow the elementary rate law, the reaction rate is expressed as

$$r_k = K_k \prod_{i,j} C_{ij}^{\nu_{ij,k}} \prod_s C_s^{\nu_{s,k}}, \quad \ldots\ldots\ldots\ldots\ldots\ldots\ldots\ldots\ldots\ldots (7)$$

where C_{ij} is the concentration of fluid component i in phase j, C_s is the concentration of solid component s, and K_k is the reaction rate constant given by

$$K_k = A_k \exp\left(-\frac{E_k}{k_B T}\right), \quad \ldots\ldots\ldots\ldots\ldots\ldots\ldots\ldots\ldots\ldots (8)$$

where E_k is the activation energy for reaction k, k_B is the Boltzmann constant, T is absolute temperature and A_k is the frequency factor for reaction k. The concentration of fluid component C_{ij} is given by

$$C_{ij} = \rho_j S_j \phi X_{ij}. \quad \ldots\ldots\ldots\ldots\ldots\ldots\ldots\ldots\ldots\ldots\ldots\ldots (9)$$

In the in-situ upgrading process, the kinetic reactions and transport equations are coupled and solved within the Newton (nonlinear) iterations. Because the fluid-component concentrations are expressed in terms of other variables in Eq. 9, when Eq. 1 is discretized, the fluid-component concentrations are not represented directly. Nonetheless, at each Newton iteration, fluid-component concentrations are updated, as are their derivatives with respect to the unknowns (here taken to be pressure, saturation, and mole fractions). In this way, the kinetic reactions are coupled fully to the other governing equations. The derivatives required to build the Jacobian matrix are presented in Appendix A.

Reaction Stoichiometry. Chemical reactions have been implemented in a generalized form in the simulator. Reactions can occur between components within a phase (gas, oil, or solid) or between components in different phases. Because of this generality, our implementation requires a larger number of stoichiometric coefficients to be entered than are required by traditional treatments [e.g., STARS (2008)]. The advantage of our approach, however, is that it allows us to define reactions as occurring between particular components within specified phases. The reaction k is represented generally by

$$\sum_i^{n_c} \sum_j^{n_p} \left(\nu'_{ij,k} - \nu_{ij,k}\right) M_{ij} + \sum_s^{n_s} \left(\nu'_{s,k} - \nu_{s,k}\right) M_s = 0, \quad \ldots\ldots\ldots\ldots (10)$$

where M_{ij} is the chemical symbol for fluid component i in phase j, M_s is the chemical symbol for solid component s, n_p is the number of fluid phases, n_c is the number of fluid components, and n_s is the number of solid components.

Kerogen is a complex mixture of large-carbon-number components. Following common practice, we represent it here in a "normalized" form (i.e., in terms of a single carbon atom), with the number of atoms of other elements scaled appropriately. The specific formula applied here is $CH_{1.5}N_{0.026}O_{0.05}$, which was used previously to represent Green River oil-shale kerogen by Braun and Burnham (1990).

We now consider a decomposition reaction from kerogen (designated KER) to other fluid components:

$$\begin{aligned} \text{KER(s)} \rightarrow\ & 0.0096\ \text{IC}_{37}\text{(o)} + 0.0178\ \text{IC}_{13}\text{ (o)} \\ & + 0.0089\ \text{IC}_{13}\text{(g)} + 0.04475\ \text{IC}_{2}\text{(g)} + 0.0054\ \text{CO}_2\text{(g)}, \end{aligned}$$

where IC indicates lumped components (explained later). In this reaction, the total number of reactive fluid components is four and the number of reactive solid components is one. Note that IC_{13}(o) and IC_{13}(g) are treated separately for purposes of reaction modeling, though they are treated as the same fluid component in the transport equations. The stoichiometric coefficients corresponding to this reaction are listed in **Table 1.** We note that the maximum number of coefficients that can be specified for any reaction is $n_p n_c + n_s$.

Heat Injection. Heat injection is the key driving force for in-situ upgrading. In this work, consistent with the actual process, we specify that the downhole heaters operate at constant temperature. In practice, accurate control of downhole temperature is essential because the upgrading reactions are very sensitive to temperature. The constant-temperature heaters are approximated here by specifying the initial temperature of gridblocks containing heaters to be the target heater temperature T_h. These blocks are also assigned very large specific-heat capacities (e.g., 10^8 Btu/lbm/°F). Our results show that this is a reasonable approach for modeling constant temperature heaters because the heater-block temperatures stay well within 1°F of T_h. A limitation of this treatment of heat injection is that we do not differentiate between heater temperature and heater-block temperature (though gridblocks in our model are quite small, typically approximately 1 ft or less in areal dimension). In reality, the heater temperature will be higher than the block temperature. Therefore, the appropriate value for T_h in our model may not coincide exactly with the value used in an actual field case. A more comprehensive treatment of heat injection will be required to model more-complex heaters that can operate under a variety of settings.

To simulate heat convection and heat conduction, the model requires representations for thermal diffusivity and component enthalpy. The rate of heat conduction is determined primarily by thermal diffusivity α, where $\alpha = \kappa/(\rho_R c_p)$. Here, ρ_R is rock density and c_p is the specific heat capacity of the rock. Thermal conductivity κ is in general a function of oil-shale grade and temperature, and ρ_R and c_p are functions of kerogen content. The values of both the rock density ρ_R and the rock specific heat c_p decrease slightly when the formation is heated and kerogen decomposes to hydrocarbons (Lee et al. 2007). For Green River oil shale that is rich in organic matter, the thermal conductivity was reported to vary between 3.5 and 8.7 Btu/ft/day/°F over a temperature range from 170 to 720°F (Nottenburg et al. 1978). In this work, we treat ρ_R and c_p as constants, though we treat κ as a history-matching parameter, which we allow to vary over the range 3.5–8.7 Btu/ft/day/°F. Thus our value for κ should be viewed as an average or "effective" value. The data we are attempting to match are those reported for Shell's pilot test, as discussed in the next section.

The enthalpy of each fluid component is represented as a function of temperature (Passut and Danner 1972):

$$H_i = H_{ai} + H_{bi} T + H_{ci} T^2 + H_{di} T^3 + H_{ei} T^4 + H_{fi} T^5, \quad \ldots\ldots\ldots (11)$$

TABLE 1—EXAMPLE OF STOICHIOMETRIC-COEFFICIENT INPUT

KER(s)	IC_{37}(o)	IC_{13}(o)	IC_2(o)	CO_2(o)	IC_{37}(g)	IC_{13}(g)	IC_2(g)	CO_2(g)
–1	0.0096	0.0178	0	0	0	0.0089	0.04475	0.0054

TABLE 2—EXAMPLE OF TIMESTEP CONTROL PARAMETERS		
Parameter	Value (No Reactions)	Value (With Reactions)
δ	0	0
ω	0.5	0.5
η for pressure	200 psi	10 psi
η for saturations	0.02	0.01
η for molar fractions	0.02	0.001

where H_i is the enthalpy of component i and H_{ai} through H_{fi} are enthalpy coefficients for component i, with the enthalpy in Btu/lbm and temperature in °R.

Solution Method. In the simulator formulation, Eqs. 1, 3, 4, 5, and 7 are discretized and solved fully implicitly. The unknowns to be computed are pressure, temperature, mole fractions of each fluid component, and solid concentrations. Volume- and composition-constraint equations are also required, which are expressed as follows:

$$\sum_j S_j = 1, \quad \sum_i X_{ij} = 1, \quad \text{for each } j. \quad \ldots\ldots\ldots\ldots\ldots\ldots (12)$$

We apply Newton's method to solve the coupled equations. After the Jacobian matrix is formed at each Newton iteration, we reduce the number of equations and variables to a set that is solved simultaneously. This reduced set of variables contains the primary variables, which represent the minimum number of unknowns needed to establish the state of the system (Cao 2002). The remaining (secondary) variables are recovered from the primary variables after each Newton iteration.

The new timestep is prescribed on the basis of changes in the unknowns over the previous timestep, as follows:

$$\Delta t^{n+1} = \Delta t^n \min\left[\frac{(1+\omega)\eta_v}{\delta_v + \omega\eta_v}\right], \quad \ldots\ldots\ldots\ldots\ldots\ldots (13)$$

where Δt^{n+1} is the next time step, Δt^n is the current timestep, ω is a tuning factor between 0 and 1, δ_v is a parameter for each variable v, η_v is the desired change for each variable, and the minimum is over all gridblocks (Cao 2002). The key parameter affecting simulator performance is the parameter η_v. Our numerical experiments show that the desired variable change when chemical reactions are present should be specified to be much smaller than in compositional simulations without reactions. This is because, when the concentration of a specific component is small (e.g., 10^{-3} lbm mol/ft^3), a desired change of 5×10^{-4} lbmol/ft^3 corresponds to a 50% change, and this may hinder convergence. Suggested parameter values for the in-situ upgrading simulations are listed in **Table 2.**

Modeling an In-situ Upgrading Demonstration Project

In this section, we describe the MDP-S and then present our detailed modeling procedure and simulation results for this project.

MDP-S. The MDP-S is a pilot in-situ conversion project conducted by Shell in the Green River formation from 2003 to 2005 (Fowler and Vinegar 2009). MDP-S is a follow-up to the original Mahagony Demonstration Project. Sixteen vertical heaters were drilled in three rings, and two producers were placed in the center of the heating pattern. One additional perimeter producer hole was drilled outside the pattern (Fowler and Vinegar 2009). Heating was conducted over a 113-ft interval. The top of this interval was at a depth of 280 ft.

Description of MDP-S Model. In order to validate our in-situ upgrading modeling capability, we developed a 3D model of MDP-S based, to the extent possible, on the information provided in Fowler and Vinegar (2009) and Vinegar (2006). As indicated earlier, much of the necessary data is proprietary, so some parameters are estimated on the basis of available publications and some are determined through history matching.

The model area is shown in **Fig. 1.** The model contains two regions, a central flow region and a surrounding heat-loss region. The central region, designated by AA' in Figs. 1a and 1b, is approximately 47 ft in diameter and 113 ft deep. This is the heated

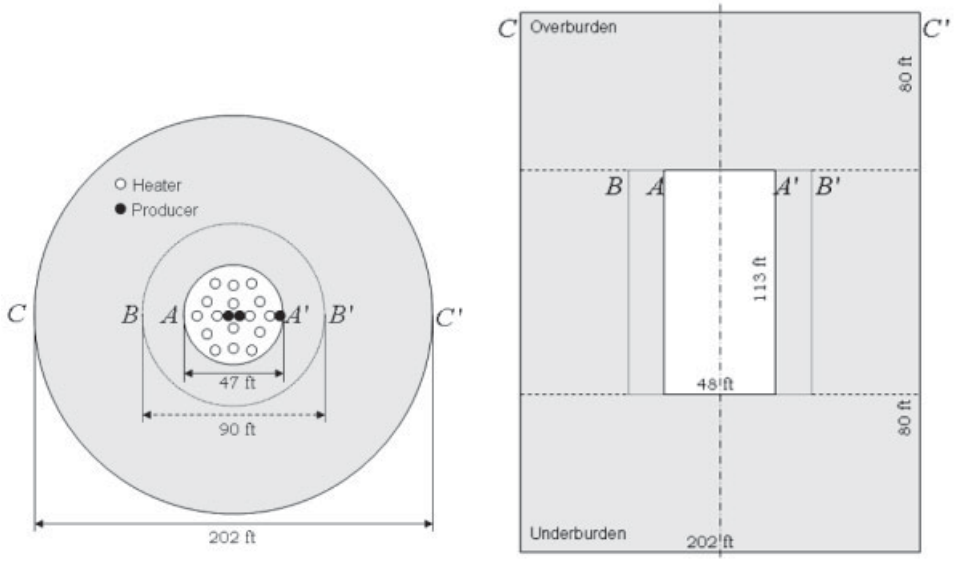

Fig. 1—Model area for MDP-S. (a) Top view. (b) Cross section.

interval. Because heat loss is a key concern in in-situ upgrading processes, a much larger heat-loss region is also included in the model. This region allows us to capture both peripheral heat loss and heat loss to the overburden and underburden. The heat-loss region is designated by *CC′* in Figs. 1a and 1b. The overall model (central flow and heat-loss regions) is approximately 202 ft in diameter and 273 ft deep.

The initial porosity and permeability of the oil-shale formation are very low (Lee et al. 2007), though, as the kerogen decomposes, both porosity and permeability increase. Reasonable values for the initial porosity and horizontal permeability are 0.0001 and 1 md, respectively, which are rounded from the data reported in Wellington et al. (2005). An appropriate value for initial vertical permeability, therefore, would be approximately 0.1 md, which accounts for a typical degree of anisotropy.

In the central flow region, we expect the porosity and permeability to be much higher than these initial values because of kerogen decomposition. As indicated, we do not model porosity and permeability evolution, so "effective" values must be assigned for these parameters in the central flow region. For a typical (rich) oil-shale formation with 15 wt% kerogen, we estimate that the porosity generated by kerogen decomposition is approximately 0.10. However, a significant fraction of the decomposition products are solids (e.g., prechar and char), and these can refill half or more of the pore space generated by kerogen decomposition. In this work, we therefore use 0.05 as the effective porosity for the central flow region. We assign the permeability for this region to be 300 md, which we calculate using the Carman-Kozeny formula presented in Wellington et al. (2005) with a value of 0.05 for porosity. Because this permeability value is, of course, just an estimate, we performed a sensitivity study to assess the effect of permeability on simulation results. We observed relatively small changes in oil and gas production for permeability over the range of 80–600 md. Therefore, our general findings can be expected to hold under the reasonable assumption that the true effective permeability is indeed within this range.

Because very little kerogen decomposes in the heat-loss region, we assign the initial porosity and permeability to the blocks in this region. Because there is very little fluid flow in the heat-loss region, the major physical process there is heat conduction. Our simulation results clearly demonstrate that the heat-loss region is sufficiently large to capture the key heat-loss effects. More specifically, as will be shown, the region boundaries remain at essentially the initial formation temperature over the course of the entire simulation, indicating that they are not affected by the downhole heaters.

Finally, we note that Fowler and Vinegar (2009) refer to the presence of pre-existing fractures in the formation. However, in the absence of quantitative data (e.g., fracture length, density, and aperture distributions), it is impossible to gauge the effects of these fractures on porosity and permeability, either before or after kerogen decomposition. Thus, we have not attempted to account for these fractures in our model of MDP-S.

Within the central flow region, we place the 16 heaters and three producers as described in Fowler and Vinegar (2009). As shown in **Fig. 2a,** the heaters are placed in three rings. The outer two rings form hexagon patterns, with heater spacing of 14 and 19.5 ft, respectively. The spacing of the four heaters in the inner ring is taken to be 10 ft. This spacing was estimated from Fig. 8 in Fowler and Vinegar (2009). The heater temperature (or specifics regarding power input) for MDP-S are not specified in Fowler and Vinegar (2009). In our simulation, we apply constant-temperature heating with T_h = 700°F. This value is within the range for target formation temperatures for in-situ upgrading processes (Biglarbigi et al. 2007). The central producers are placed 5 ft apart, and the perimeter producer is located 4 ft south of the southern-most heater. All producers are specified to operate with a bottomhole pressure of 30 psi. We represent the system using a polar grid, shown in Fig. 2b. Because of symmetry, we model only half of the region and then multiply the total production data by two to obtain full-field results. A limited grid-refinement study demonstrated that the general level of grid resolution used here is sufficient.

Model Components, Reactions, and Other Parameters. Modeling of the in-situ upgrading process for MDP-S requires phase-component data, chemical-kinetics data, initial formation conditions, and thermal properties of the rock. We now describe our models for these data.

The reactions included in the model were determined on the basis of data provided by Wellington et al. (2005). Because these

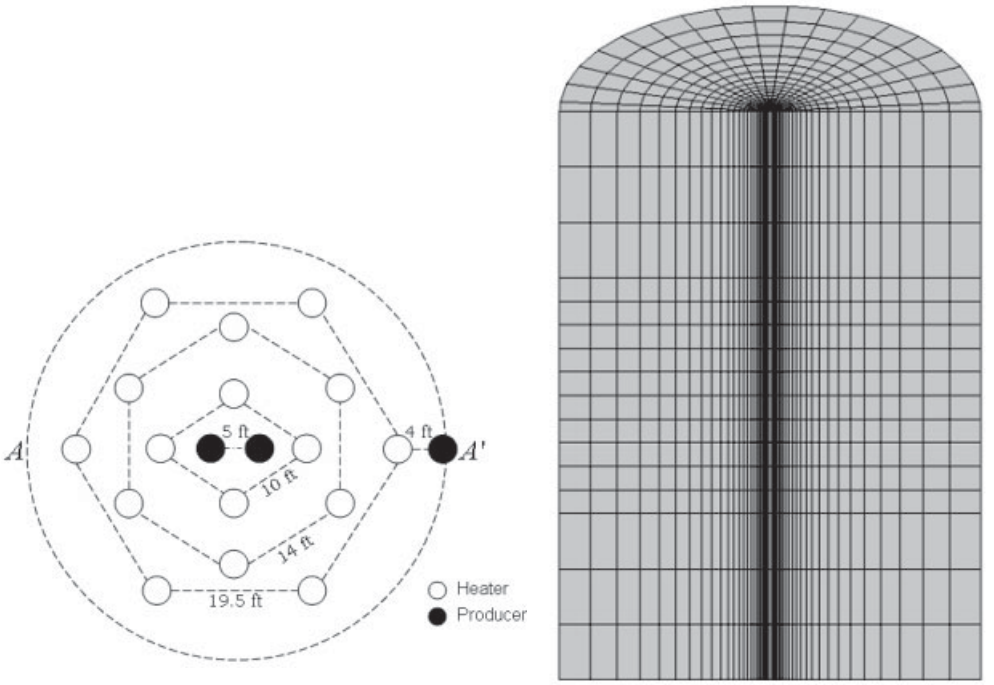

Fig. 2—(a) Heater and well positions and (b) gridding of the MDP-S simulation model.

TABLE 3—KINETIC REACTIONS IN MDP-S CASE*

Number	Reactions	Frequency Factor	Activation Energy (kJ/mol)
1	KER(s) $\longrightarrow$ 0.0096 IC_{37}+0.0178 IC_{13}+0.04475 IC_2+0.00541 CO_2	3.74×10^{12}	161.600
2	IC_{37} (g) $\longrightarrow$ 1.853 IC_{13}+ 0.045 IC_2	2.65×10^{20}	206.034
3	IC_{37} (o) $\longrightarrow$ 0.2063 IC_{13}+ 2.365 IC_2	6.25×10^{16}	206.034
4	IC_{13} (g) $\longrightarrow$ 5.73 IC_2	3.82×10^{20}	219.328
5	IC_{13} (o) $\longrightarrow$ 0.573 IC_2	9.85×10^{16}	219.328

*Adapted from Wellington et al. (2005)

reactions are defined in terms of generic components (e.g., heavy oil, light oil, hydrocarbon gas), whose properties are not defined, we must relate these pseudocomponents to actual components and then apply lumping procedures to determine properties. We proceed as follows.

The reactions included in the model and the associated kinetic data are listed in **Table 3.** We use pseudospecies IC_{37} to represent heavy oil, IC_{13} to represent light oil, and IC_2 to represent the hydrocarbon gas referred to in Wellington et al. (2005). The reactions in Table 3 were modified slightly from those presented in Wellington et al. (2005). Specifically, we eliminated water and prechar from the reactions (water is not included in our model, and prechar is assumed to stay in the solid phase, as discussed previously). In addition, we combined the two parallel kerogen-decomposition reactions in Wellington et al. (2005) to one reaction (Reaction 1 in Table 3). Our numerical results show that this combination reduces computation time and does not affect hydrocarbon-production rates. The reactions in Table 3 are not in exact element balance because we do not include the prechar and char products, which are not considered in the transport equations. This imbalance is not a problem because this mass originates from the solid phase, which is treated as the hydrocarbon source.

The components used in our model are taken from the pyrolysis analysis of Green River oil shale in Braun and Burnham (1990). These experiments identified 31 components, consisting of 22 oil species and nine gas species. As a simplification, we consider only the 11 most abundant oil species and the four most abundant gas species. Because the available set of kinetics data (Table 3) is in terms of only three hydrocarbon species, we performed a component-lumping process to map the 13 hydrocarbon species to the three pseudocomponents appearing in Table 3. The original components and the lumped pseudocomponents used in the model are listed in **Table 4.** The gas species CH_4 and CH_x were lumped to one component and mapped to pseudospecies IC_2, the oil species Oil 1 through Oil 6 were lumped and mapped to IC_{13}, and the oil species Oil 7 through Oil 11 were lumped and mapped to IC_{37}. The interaction coefficients for these lumped components, for use in the EOS, are provided in **Table 5.** The enthalpy coefficients for the individual oil and gas species are determined from Passut and Danner (1972). Enthalpy coefficients for the lumped components are listed in **Table 6.** The lumping process was accomplished using the software package WinProp (WinProp 2008). The other parameters used in the MDP-S simulation are given in **Table 7** (two of these parameters are established through history matching, as described later).

TABLE 4—COMPOSITIONS AND PROPERTIES: GREEN RIVER SHALE PYROLYSIS AND LUMPED COMPONENTS

Species Name	Molar Weight (g/mol)	Critical Pressure (psi)	Critical Temperature (R)	Accentric Factor
Pyrolysis Components From Green River Oil Shale*				
CO_2	44.01	1,070.40	547.53	0.239
N_2	28.01	491.68	227.13	0.039
CH_4	16.04	667.18	342.33	0.011
CH_x	44.10	616.42	666.33	0.153
Oil 1	86	493.14	979.53	0.227
Oil 2	114	426.42	1,103.73	0.300
Oil 3	142	374.20	1,218.93	0.307
Oil 4	177	333.59	1,323.33	0.379
Oil 5	212	292.98	1,413.33	0.426
Oil 6	261	253.82	1,506.93	0.511
Oil 7	317	213.21	1,595.13	0.594
Oil 8	380	174.05	1,674.33	0.664
Oil 9	464	133.44	1,751.73	0.762
Oil 10	562	92.82	1,793.13	0.941
Oil 11	703	92.82	1,830.93	1.31
Components and Lumped Components**				
CO_2	44.01	1070.40	547.53	0.239
N_2	28.01	491.68	227.13	0.039
IC_2	30.07	668.48	519.74	0.008
IC_{13}	169.52	348.82	1,287.65	0.365
IC_{37}	465.83	135.69	1,732.11	0.818

*From Braun and Burnham (1990).
**IC represents lumped pseudocomponent.

TABLE 5—INTERACTION COEFFICIENTS FOR COMPONENTS

	CO_2	N_2	IC_2	IC_{13}	IC_{37}
CO_2	0	0.00003	0.00411	0.04309	0.1006
N_2	0.00003	0	0.0035	0.04561	0.10602
IC_2	0.00411	0.0035	0	0.02462	0.07449
IC_{13}	0.04309	0.04561	0.02462	0	0.0150
IC_{37}	0.1006	0.10602	0.07449	0.0150	0

The pore space of oil-shale formations can initially be saturated with brine or gases. Here, we specify the pore space to be initially saturated with nitrogen and carbon dioxide. These gases are produced from the central producer at early time. As the kerogen decomposes, the pore space becomes saturated with hydrocarbons. As discussed, we do not include porosity and permeability evolution in our model.

The parameters described earlier are treated as fixed. Two other parameters in the model, initial kerogen concentration and thermal conductivity, are treated as adjustable parameters because they are not reported. Data are available, however, that prescribe reasonable physical ranges for these quantities. Commercially feasible oil-shale deposits contain between approximately 10 and 20 wt% kerogen (Dyni 2006). The density of oil shale is approximately 2 g/cm^3, so the kerogen content should be approximately 0.2–0.4 g kerogen/cm^3 oil shale. Given that we represent kerogen as $CH_{1.5}N_{0.026}O_{0.05}$, this range corresponds to 0.85–1.7 lbm mol/ft^3. Thermal conductivity was reported to vary from 3.5 to 8.7 Btu/ft/day/°F for organic-rich oil-shale formations (Nottenburg et al. 1978).

We varied the initial kerogen concentration and thermal conductivity over these physical ranges to establish a reasonable level of agreement between our simulation results and the MDP-S pilot data. The parameter values thus determined are 1.3 lbm mol/ft^3 for the initial kerogen concentration and 7 Btu/ft/day/°F for the rock thermal conductivity. Using these parameters, the model predicts total oil production of 1,834 bbl and total hydrocarbon production of 2,529 bbl of oil equivalent (BOE) after 500 days of production (in computing BOE, we take 5.478 Mcf of gas to be equivalent to 1 bbl of oil). The reported field-test results are 1,813 bbl of oil and 2,659 BOE, respectively (Vinegar 2006). Thus, the simulation predictions for total production are within 5% of the field-test results.

Although these MDP-S model parameters are physically realistic, this "history match" is, of course, nonunique, and it is likely that other sets of parameters would provide comparable agreement with the field data. We further expect that the level of agreement could be improved by treating more parameters as adjustable (e.g., effective porosity and permeability). Nonetheless, the fact that we are able to achieve acceptable agreement with the test results using realistic parameter values provides a degree of validation for our implementation.

Simulation Results. The oil- and gas-production results for the MDP-S case are shown in **Figs. 3a and 3b.** Fig. 3a illustrates some characteristics of the in-situ upgrading process. The initial high gas-production rate is because of the decomposition of the kerogen in the heater blocks—this kerogen breaks down quickly after the simulation starts (the heaters are operated at a temperature of 700°F). The reservoir temperature then gradually increases, and both gas and oil production ramp up approximately 50 days after heat injection is initiated. Peak hydrocarbon production is reached at approximately 220 days. Then, as the kerogen is consumed, oil- and gas-production rates decrease.

TABLE 7—SUMMARY OF INPUT PARAMETERS USED IN MDP-S MODEL

Parameter	Value
Grid (n_r, n_θ, n_z)	(33, 19, 16)
Overburden thickness	80 ft
Heated interval	113 ft
Underburden thickness	80 ft
Initial temperature	70°F
Initial pressure	101 psi
Initial kerogen	1.3 lbmol/ft^3
Rock compressibility	3×10^{-6}/psi
Porosity (heat loss region)	0.0001
Permeability (heat loss region)	$k_r = k_\theta = 10\ k_z = 1$ md
Porosity (central flow region)	0.05
Permeability (central flow region)	$k_r = k_\theta = k_z = 300$ md
Thermal conductivity	7 Btu/ft/day/°F
Heater temperature	700°F
Producer BHP	30 psi
Rock volumetric heat capacity	25 Btu/ft^3/°F

As discussed, the porosity was set to 0.0001 in the heat-loss regions. Because this low value for porosity necessitates small timesteps and, thus, leads to high computation times, we investigated the effect of deactivating the cells in the heat-loss regions with respect to flow by setting permeability to zero (these cells are still active in terms of heat conduction). Simulation results for this case are very similar to those for the previous case (e.g., kerogen concentration maps are essentially identical and there is only a difference of 0.2% in total hydrocarbon production between the two cases). By deactivating these cells, however, we achieved a speedup factor of two relative to the previous case. Therefore, in all of the following simulations, we consistently set permeability to zero in the heat-loss regions.

Fig. 4 shows a cross-sectional view of the temperature in the MDP-S model after 500 days of heat injection. Most of the central flow region is above 600°F except for the portion adjacent to the surrounding heat-loss region. The simulation results indicate that the temperature change far from the heater patterns is not significant. In the figures that follow, therefore, we show only the central flow region and a small portion of the heat-loss region. This region is designated as *BB′* in Fig. 1a.

Figs. 5a through 5c depict the formation temperature, kerogen concentration, and oil saturation, respectively, at various times during the in-situ upgrading process. The heating of the central flow region is evident from Fig. 5a. From Fig. 5b, we

TABLE 6—ENTHALPY COEFFICIENTS FOR EACH LUMPED COMPONENT

	CO_2	N_2	IC_2	IC_{13}	IC_{37}
H_{ai}, Btu·lbm^{-1}	4.78	-6.89×10^{-1}	–3.40	0.00	0.00
H_{bi}, Btu·lbm^{-1}·(°R)$^{-1}$	1.14×10^{-1}	2.54×10^{-1}	3.73×10^{-1}	-5.97×10^{-2}	-1.56×10^{-2}
H_{ci}, Btu·lbm^{-1}·(°R)$^{-2}$	1.01×10^{-4}	-1.45×10^{-5}	-1.08×10^{-4}	4.01×10^{-4}	3.90×10^{-4}
H_{di}, Btu·lbm^{-1}·(°R)$^{-3}$	$-2.65\text{E}\times10^{-8}$	1.25×10^{-8}	3.34×10^{-7}	-6.22×10^{-8}	-5.56×10^{-8}
H_{ei}, Btu·lbm^{-1}·(°R)$^{-4}$	$3.47\text{E}\times10^{-12}$	-1.71×10^{-12}	-1.39×10^{-10}	0.00	0.00
H_{fi}, Btu·lbm^{-1}(°R)$^{-5}$	-1.31×10^{-16}	-8.24×10^{-17}	1.93×10^{-14}	0.00	0.00

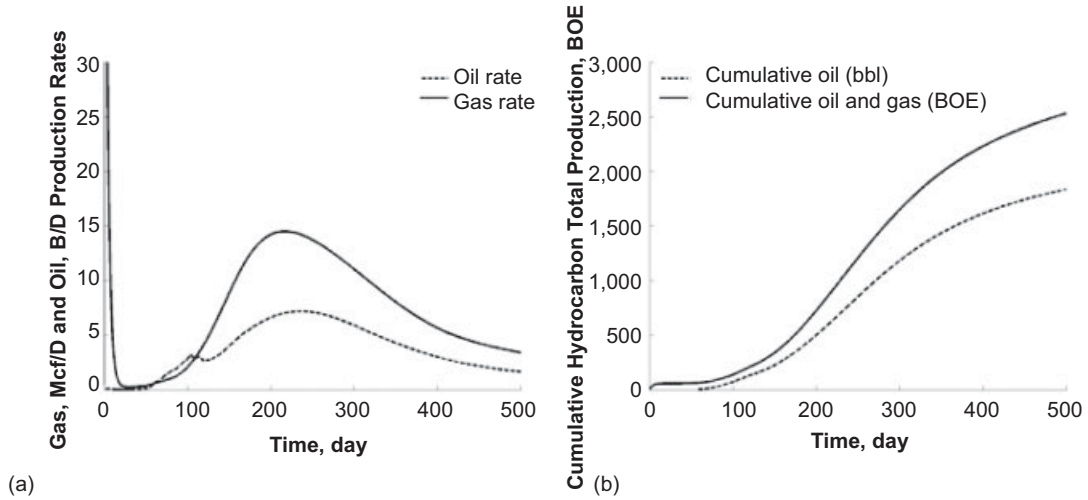

Fig. 3—Hydrocarbon-production results from MDP-S model. (a) Oil and hydrocarbon gas production rates. (b) Cumulative oil and total hydrocarbon production.

see that kerogen first decomposes near the heaters and eventually throughout the entire heated region. After 500 days, the kerogen is almost fully depleted. At 60 days, the oil-saturation map (Fig. 5c) is approximately the inverse of the kerogen map, except that the oil is affected by gravity. The producers are completed at the bottom of the heated interval, so it is from here that oil and gas are produced. Fig. 5c also shows that the oil within the heating pattern is completely produced at 500 days. However, some oil just outside the heating pattern has not yet been produced. This is because the viscosity of this oil is higher because of the lower temperature in this region.

Overall oil- and gas-production rates are shown in Figs. 3a and 3b. It is, however, also of interest to consider the composition of the produced oil and gas. These compositions are presented in **Fig. 6.** Here, we see that the largest gas component is IC_2 and the largest oil component is IC_{13}. The production rate of the heavy-oil species IC_{37} in both the gas and oil phases is close to zero because this component decomposes very quickly once it is generated. The overall produced oil can be classified as high-quality light oil, with an average API gravity of 45. This value, of course, is strongly dependent on the components lumped into IC_{13}. It is of interest to note that the API gravity of the MDP-S oil is also reported to be 45 (Vinegar 2006).

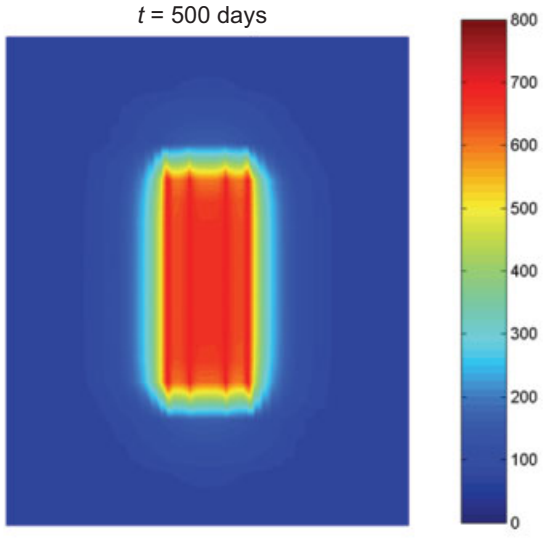

Fig. 4—Cross section of temperature (°F) at 500 days (region between *CC'* in Fig. 1b shown).

Sensitivity Analysis

We now assess the sensitivity of the in-situ upgrading procedure to key engineering parameters, specifically heater temperature, heater pattern, and heater spacing. For this assessment, we model infinite systems containing repeated patterns of heaters and producers. For such models, we need only simulate a single symmetry element (or a portion of a symmetry element). The patterns considered are shown in **Figs. 7a through 7c.** The base case here is the hexagonal heater arrangement (Fig. 7a), with the heaters operated at a constant temperature of 700°F. The heater spacing is 8 ft. The simulation area within one hexagon pattern in the base case is approximately 183 ft^2. The thickness of the overburden and underburden are both 80 ft (these are included to account for heat loss). We use Cartesian grids with cell dimensions $\Delta x = \Delta y = 0.5$ ft and $\Delta z = 11.3$ ft in the heated interval and $\Delta z = 26.7$ ft in the overburden and underburden. A limited grid-refinement study showed that production results are insensitive to further refinement. Peripheral heat loss does not occur in any of the sensitivity cases because the patterns are considered to be repeated indefinitely. Except where otherwise specified, the other model parameters are the same as those used in the MDP-S simulation discussed previously.

Temperature Effect. We first consider the effect of heater temperature on the in-situ upgrading process. For these results, we consider only the hexagon pattern. Because of symmetry, we simulate half of the pattern and then reconstruct results for the full pattern (in all cases, we report results for the full pattern). Temperature results for the base case (T_h = 700°F) are shown in **Fig. 8a.** We also considered T_h = 650°F and T_h = 600°F. Results for the latter case appear in Fig. 8b. As expected, formation temperatures are consistently lower for the T_h = 600°F case.

Results for gas and oil rates and cumulative production for the three cases are presented in **Fig. 9.** We observe that the hydrocarbon production is very sensitive to temperature—with these decreases in T_h, the peak oil and gas rates decrease significantly. The peak production times are also delayed, and the peaks are not as sharp, as the heater temperature decreases. This is because of the strong dependency of the reaction rates on temperature. In addition, at lower T_h, the cumulative hydrocarbon production is consistently below that for the base case over the entire simulation. This is again because of the slower kinetics. The ultimate production for all three cases is expected to be the same if the simulations were run for very long times.

Heater-Pattern Effect. We now evaluate the effect of heater pattern by considering two additional cases—a square heater pattern and a triangular heater pattern, as shown in Figs. 7b and 7c, respectively. All parameters are otherwise the same as in the base

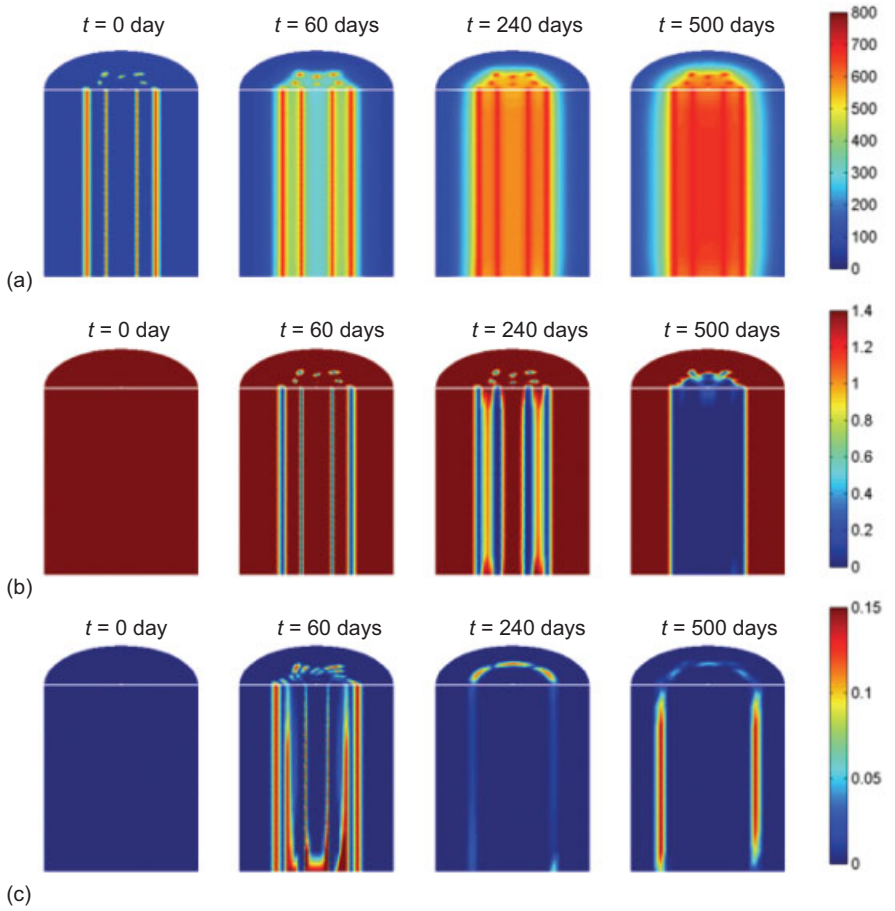

Fig. 5—MDP-S simulation results over region BB′ (shown in Fig. 1b). (a) Temperature (°F). (b) Remaining kerogen (lbm mol/ft³). (c) Oil saturation.

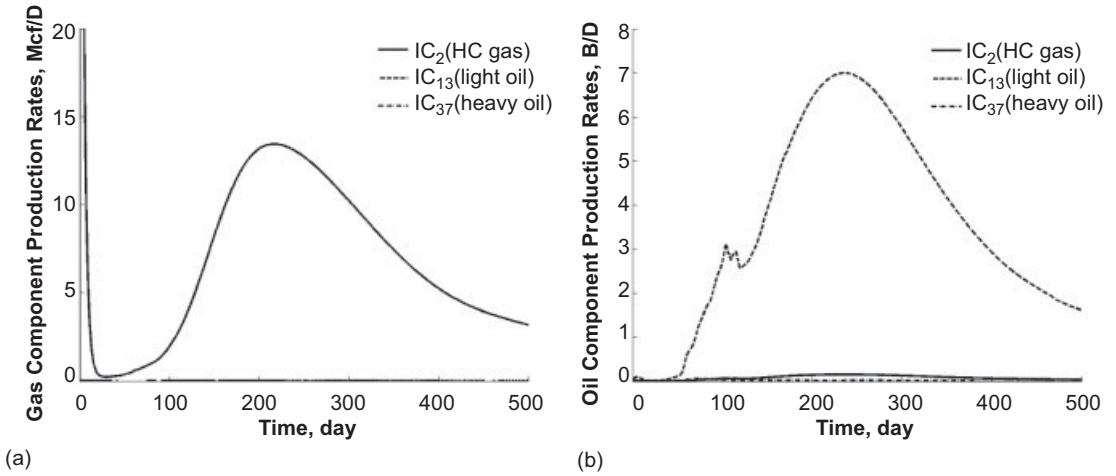

Fig. 6—Hydrocarbon component production rates from MDP-S model. (a) Gas component rates. (b) Oil component rates.

case (e.g., T_h = 700°F). These patterns contain fewer heaters than the base case, but the total areas of all three patterns are essentially the same (within a few percent). The heater spacing is 13 ft in the square pattern and 20 ft in the triangular pattern.

Temperature results for the square and triangle patterns, respectively, are shown in Figs. 8c and 8d. Production results for these patterns, along with those of the base case, are presented in **Fig. 10.** As would be expected, with fewer heaters per volume of oil shale, more time is required for the formation temperature to approach T_h (compare Figs. 8a, 8c, and 8d), and the peak production times for both oil and gas are correspondingly delayed. It is also evident that, during the 2,000 days of simulation, the cumulative hydrocarbon

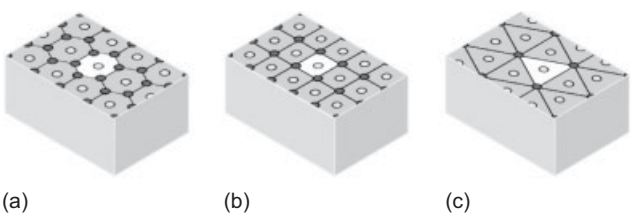

Fig. 7—Top view of heaters and producers for sensitivity analysis. (a) Hexagon pattern. (b) Square pattern. (c) Triangle pattern.

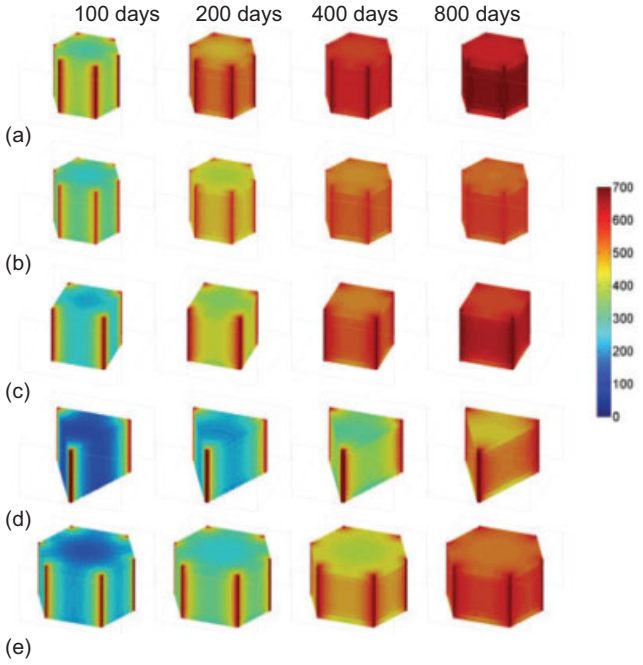

Fig. 8—Temperature variation for cases in sensitivity analysis. (a) Repeated hexagon pattern (heater temperature is 700°F, heater spacing is 8 ft; this model represents the base case). (b) Repeated hexagon pattern (heater temperature is 600°F, heater spacing is 8 ft). (c) Repeated square pattern (heater temperature is 700°F, heater spacing is 13 ft). (d) Repeated triangle pattern (heater temperature is 700°F, heater spacing is 20 ft). (e) Repeated hexagon pattern (heater temperature is 700°F, heater spacing is 12 ft).

production for the square and triangle patterns is always lower than that for the hexagon pattern.

These results are of interest because they illustrate the sorts of tradeoffs that must be considered in designing a field-scale in-situ upgrading process. Specifically, the triangle pattern entails fewer heaters, so it will be less expensive to implement. The oil and gas produced from this pattern are delayed considerably, however, relative to that produced from the more expensive hexagon pattern; thus, the value of the hydrocarbons produced from the triangle pattern must be discounted. The relative advantages and disadvantages of these and other patterns can best be assessed through a systematic study. It will also be useful to apply formal optimization strategies to this problem.

Heater-Spacing Effect. The effect of the distance between adjacent heater wells is now studied by considering two additional cases for the hexagon pattern. The heater spacings in these cases are 10 and 12 ft. We note that the simulation areas increase when the heater spacing is increased. All other system parameters are the same as in the base case. The temperature variation for the case with 12-ft spacing is shown in Fig. 8e. Results for hydrocarbon production are shown in **Fig. 11.** We observe that increases in heater spacing have a noticeable effect on reservoir temperature. Peak oil and gas production occurs later, and the peaks are less sharp than in the base case (similar effects were observed for the square and triangle patterns). With larger heater patterns, more total kerogen is available, though the decomposition requires more time. The ultimate cumulative hydrocarbon production in these cases is proportional to the pattern area. However, because of heat loss to the underburden and overburden, larger heater spacing requires more total energy input (per energy produced) than smaller spacings. We quantify this effect in the next section.

Energy Ratios for the Various Scenarios. A key efficiency measure for the in-situ upgrading process (or for any production operation that requires very substantial energy input) is the ratio of energy produced to energy expended. This ratio, which we refer to as E_{out}/E_{in}, should be significantly larger than unity for a cost-effective operation. Here, we measure energy output as the chemical energy content of the cumulative hydrocarbon production, with each barrel of oil equivalent yielding 5.6×10^6 Btu. The energy input considered here includes only thermal energy—we do not account for energy losses associated with generating the electricity required to power the heaters. Because we use very large specific-heat capacities for the heater blocks, the internal energy in the heater blocks at initial time is very large. Over the course of the simulation, thermal energy diffuses from heater blocks to the formation. The thermal energy introduced into the formation is computed from the total energy decrease in the heater blocks:

$$E_{in} = \sum_{h=1}^{n_h} \left(E_h^0 - E_h \right), \quad \ldots\ldots\ldots\ldots\ldots\ldots\ldots\ldots\ldots\ldots\ldots\ldots (14)$$

where h is heater block index, n_h is the number of heater blocks, E_h is the total internal energy in heater block h, and E_h^0 is the initial heater-block energy.

In practice, it will not be economic to operate an in-situ upgrading process once hydrocarbon production falls below some threshold. Here, we assume that production proceeds until 90% of the hydrocarbons are produced. The total hydrocarbon production is computed on the basis of a Fischer assay of the kerogen. This

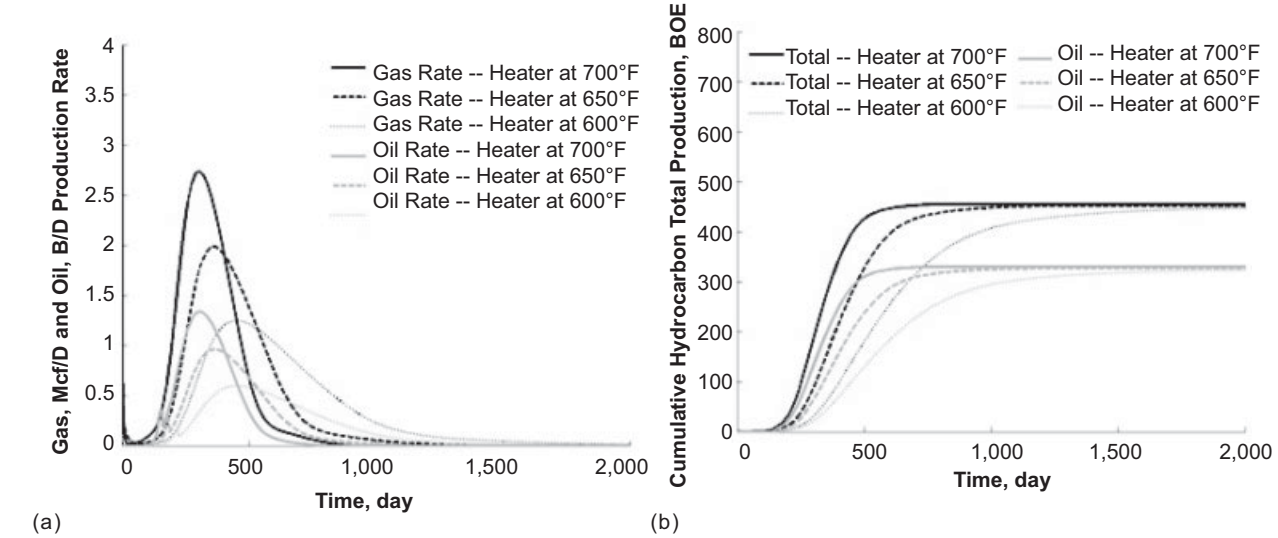

Fig. 9—Effect of heater temperature on production. (a) Oil and gas hydrocarbon production rates. (b) Cumulative oil and total hydrocarbon production.

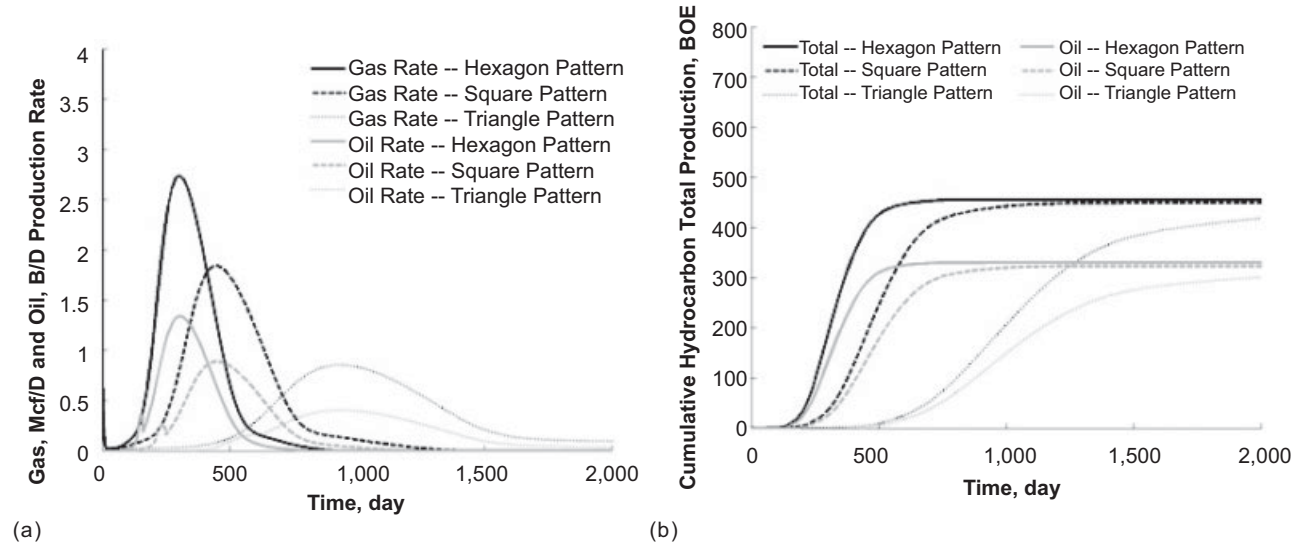

Fig. 10—Effect of heating pattern on production. (a) Oil and gas hydrocarbon production rates. (b) Cumulative oil and total hydrocarbon production.

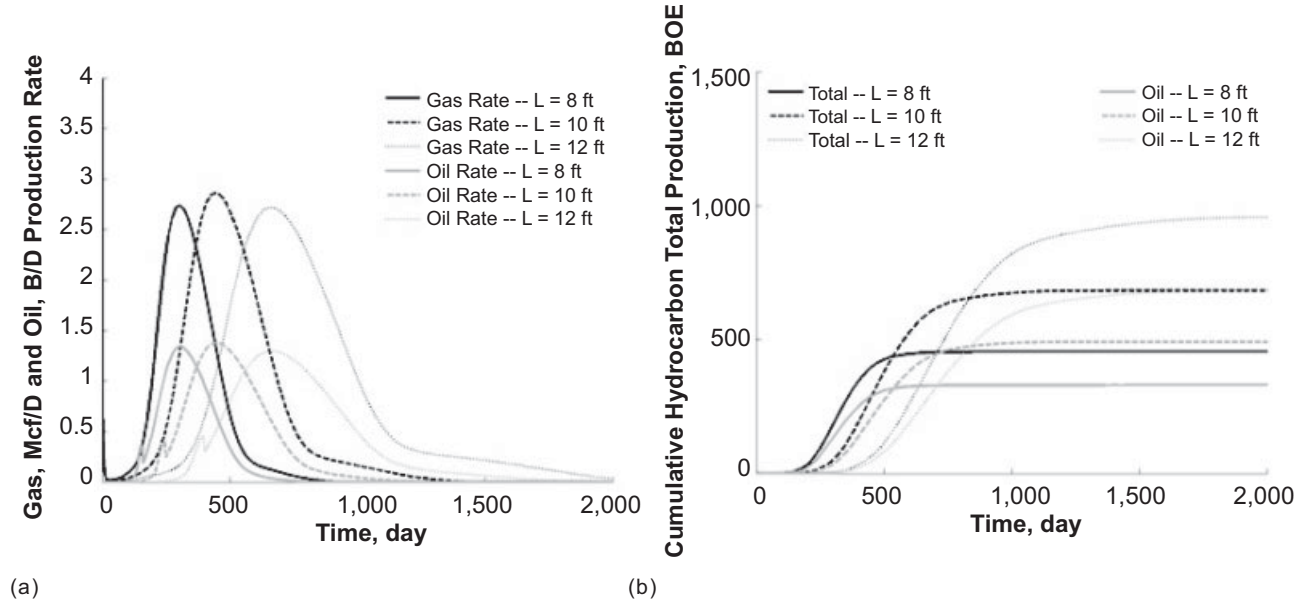

Fig. 11—Effect of heater spacing on production. (a) Oil and gas hydrocarbon production rates. (b) Cumulative oil and total hydrocarbon production.

means that different scenarios will operate for different periods of time. This procedure for computing E_{out}/E_{in} will generally benefit scenarios in which hydrocarbon production occurs quickly and shows sharp (rather than diffused) peaks.

Results for E_{out}/E_{in} are presented in **Table 8.** These energy ratios fall within a range of 6.2–6.9. The highest energy ratio is obtained for the base case and for the hexagon pattern with 8-ft heater spacing and T_h = 650°F. The results in Table 8 indicate that the energy ratio decreases when the heater spacing increases. This can be explained in terms of heat loss to the overburden and underburden because prolonged operating time results in increased energy loss.

TABLE 8—ENERGY RATIOS FOR CASES CONSIDERED IN THE SENSITIVITY STUDY*

Pattern	Heater Temperature	Heater Spacing	Thermal Energy Input (Btu)	Chemical Energy Output (Btu)	E_{out}/E_{in}
Hexagon	700°F	8 ft	3.346×10^{8}	2.296×10^{9}	6.9
Hexagon	650°F	8 ft	3.345×10^{8}	2.296×10^{9}	6.9
Hexagon	600°F	8 ft	3.367×10^{8}	2.296×10^{9}	6.8
Square	700°F	13 ft	3.396×10^{8}	2.283×10^{9}	6.7
Triangle	700°F	20 ft	3.646×10^{8}	2.261×10^{9}	6.2
Hexagon	700°F	10 ft	5.175×10^{8}	3.480×10^{9}	6.7
Hexagon	700°F	12 ft	7.560×10^{8}	4.914×10^{9}	6.5

*At 90% recovery efficiency.

It is of interest to compare these values with those computed by Brandt (2008), who performed a high-level (system) analysis of the in-situ upgrading process. In his paper, Brandt considered a number of effects not included here, such as energy losses associated with electricity generation, so his values for E_{out}/E_{in} are much lower than those in Table 8. Considering only thermal-energy inputs, as in the energy-ratio results presented here, Brandt (personal communication) arrived at values for E_{out}/E_{in} of 6.1–7.4, which are in close agreement with the results presented in Table 8. This lends further credence to our in-situ upgrading modeling capability. Finally, we note that the existence of significant amounts of in-situ water will act to reduce E_{out}/E_{in} because energy must be expended to heat and vaporize this water. This effect is not included in our model.

Conclusions

In this paper, we described the development of a simulator capable of modeling in-situ upgrading processes. The implementation was accomplished within the framework of Stanford's GPRS. The overall model includes chemical kinetics fully coupled with a thermal/compositional formulation. The new capability was applied to simulate a system based on Shell's in-situ upgrading pilot test, the MDP-S. These simulations used Green River oil-shale data, 16 heaters, and three producers. The downhole heaters were simulated as constant-temperature heat sources. After modest tuning of some uncertain system parameters, the results from our model demonstrated reasonable agreement with data reported for the field test. This provides a degree of validation for the in-situ upgrading simulation capability.

A sensitivity analysis showed that the oil and gas production are highly dependent on the heater temperature. Through a range of 600–700°F, higher heater temperature was shown to provide faster overall hydrocarbon production. Heater pattern can also affect oil- and gas-production rates and cumulative production. The hydrocarbon yield is additionally affected by the distance between adjacent wells. The ratio of energy output to energy input was found to be in the range of 6.2–6.9 for all sensitivity cases considered. This ratio is affected by heat loss to the overburden and underburden. In total, we believe that the simulation procedure developed here may, after further validation and extension, find use in the design and optimization of in-situ upgrading processes.

Nomenclature

A = frequency factor
b = viscosity coefficient
c = viscosity coefficient
c_p = rock specific-heat capacity, Btu/lbm/°F
C = concentration, lbm mol/ft^3
D = depth, ft
E = activation energy, Btu/lbm mol [kJ/mol]
E_{in} = thermal-energy input, Btu
E_{out} = chemical-energy output, Btu
f = fugacity
F = mass- or energy-balance equation residual
g = gravitational acceleration
H = enthalpy, Btu/lbm mol [Btu/lbm]
$\mathbf{K}$ = permeability tensor, md
K = reaction constant
M = chemical symbol
n_c = number of fluid components
n_h = number of heater blocks
n_p = number of fluid phases
n_s = number of solid components
p = pressure, psi
q^H = energy source term, Btu/day
q^W = well source term, ft^3/day
r = reaction rate, lbm mol/ft^3/day
R = reaction term
s = viscosity coefficient
S = saturation
t = time, day
T = temperature, °F[°C, °R]
$\mathbf{u}$ = Darcy velocity, ft/day
U = internal energy, Btu
V = gridblock volume, ft^3
X = fluid component molar fraction
α = thermal diffusivity, ft^2/day
δ = tuning factor for timestep control
η = desired variable change
κ = thermal conductivity, Btu/ft/day/°F
μ = viscosity, cp
ν = stoichiometric coefficient
ρ = density, lbm mol/ft^3 [lbm/ft^3]
ϕ = porosity
ω = tuning factor for timestep control

Superscripts

g = gas phase
n = timestep
o = oil phase
W = well

Subscripts

c = variable index
e = energy equation
h = heater-block index
i = fluid-component index
j = fluid-phase index
k = chemical-reaction index
r = relative permeability
R = rock
s = solid-component index
v = unknown variable index
α = target fluid-component index
β = target fluid-phase index
χ = target solid-component index

Constant

k_B = Boltzmann constant, 1.3806503×10^{-23} kg m^2/s^2/K

Acknowledgments

We are grateful to the industrial affiliates of the Stanford University Reservoir Simulation Research Consortium (SUPRI-B) for partial funding. We also thank Adam Brandt for valuable suggestions and for pointing us to useful references.

References

Biglarbigi, K., Dammer, A., Cusimano, J., and Mohan, H. 2007. Potential for Oil Shale Development in the United States. Paper SPE 110590 presented at the SPE Annual Technical Conference and Exhibition, Anaheim, California, USA, 11–14 November. doi: 10.2118/110590-MS.

Brandt A.R. 2008. Converting Oil Shale to Liquid Fuels: Energy Inputs and Greenhouse Gas Emissions of the Shell in Situ Conversion Process. *Environ. Sci. Technol.* **42** (19): 7489–7495. doi: 10.1021/es800531f.

Braun R.L. and Burnham A.K. 1990. Mathematical Model of Oil Generation, Degradation, and Expulsion. *Energy & Fuels* **4** (2): 132–146. doi: 10.1021/ef00020a002.

Burnham A.K. and Braun R.L. 1984. General Kinetic Model of Oil Shale Pyrolysis. Report UCRL-89805, Lawrence Livermore National Laboratory, Livermore, California.

Burnham A.K. and Braun R.L. 1993. Chemical Reaction Model for Oil and Gas Generation from Type I and Type II Kerogen. Report UCRL-ID-114143, Lawrence Livermore National Laboratory, Livermore, California.

Cao, H. 2002. Development of Techniques for General Purpose Simulators. PhD thesis, Stanford University, Stanford, California.

Crawford, P.M., Biglarbigi, K., Dammer, A.R., and Knaus, E. 2008. Advances in World Oil Shale Technologies. Paper SPE 116570 presented

at the SPE Annual Technical Conference and Exhibition, Denver, 21–24 September. doi: 10.2118/116570-MS.

Dyni, J.R. 2006. Geology and Resources of Some World Oil-Shale Deposits. Scientific Investigations Report 2005-5294, US Geological Survey, Reston, Virginia (posted June 2006).

Fowler, T.D. and Vinegar, H.J. 2009. Oil Shale ICP—Colorado Field Pilots. Paper SPE 121164 presented at the SPE Western Regional Meeting, San Jose, California, USA, 24–26 March. doi: 10.2118/121164-MS.

Jiang, Y. 2008. Techniques for Modeling Complex Reservoirs and Advanced Wells. Ph.D. dissertation, Stanford University, Stanford, California.

Jossi, J.A., Steil, L.I., and Thodos, G. 1962. The Viscosity of Pure Substances in the Dense Gaseous and Liquid Phases. *AIChE Journal* **8** (1): 59—63. doi: 10.1002/aic.690080116.

Lake, L.W. 1989. *Enhanced Oil Recovery*. Englewood Cliffs, New Jersey: Prentice Hall.

Lee S., Speight J.G., and Loyalka S.K. 2007. *Handbook of Alternative Fuel Technologies*. Boca Raton, Florida: CRC Press.

Miadonye, A., Singh, B., and Puttagunta, V.R. 1994. Modeling the Viscosity-Temperature Relationship of Alberta Bitumens. *Fuel Sci. and Tech. International* **1**2 (2): 335–350. doi: 10.1080/08843759408916182.

Nottenburg, R., Rajeshwar, K., Rosenvold, R., and DuBow, J. 1978. Measurement of Thermal Conductivity of Green River Oil Shales by a Thermal Comparator Technique. *Fuel* **57** (12): 789–795. doi: 10.1016/0016-2361(78)90141-2.

Pan, Z., Feng, H.Y., and Smith, J.M. 1984. Rates of Pyrolysis of Colorado Oil Shale. *AIChE Journal* **31** (5): 721–728. doi: 10.1002/aic.690310504.

Passut, C.A. and Danner, R.P. 1972. Correlation of Ideal Gas Enthalpy, Heat Capacity, and Entropy. *Ind. Eng. Chem. Process Des. Dev.* **11** (4): 543–546. doi: 10.1021/i260044a016.

Peters, K.E., Walters, C.C., and Moldowan, J.M. 2005. *The Biomarker Guide, Volume 2: Biomarkers and Isotopes in Petroleum Exploration and Earth History*, second edition. Cambridge, UK: Cambridge University Press.

STARS User Manual. 2008. Calgary, Alberta: Computer Modelling Group (CMG).

Vinegar, H. 2006. Shell's In-situ Conversion Process. Presented at the Colorado Energy Research Institute 26th Oil Shale Symposium, Golden, Colorado, USA, 16–18 October. Downloaded 31 October 2008 from http://www.ceri-mines.org/documents/R05a-HaroldVinegar.pdf.

Wellington, S.L., Berchenko, I.E., Rouffgnac, E.P., Fowler, T.D., Ryan, R.C., Shahlin, G.T., Stegemeier, G.L., Vinegar, H.J., and Zhang, E. 2005. In Situ Thermal Processing of an Oil Shale Formation To Produce a Desired Product. US Patent No. 6,880,633.

WinProp User Manual. 2008. Calgary, Alberta: Computer Modelling Group (CMG).

Appendix A—Implementation

The kinetic-reaction terms in Eqs. 1 and 3, here denoted as R_i and R_s, are given by

$$R_i = V\sum_{j=1}^{n_p}\sum_{k=1}^{n_k}\left(\nu'_{ij,k}-\nu_{ij,k}\right)r_k, \text{ (for fluid component } i) \quad \ldots\ldots\ldots (A\text{-}1)$$

and

$$R_s = V\sum_{k=1}^{n_k}\left(\nu'_{s,k}-\nu_{s,k}\right)r_k, \text{ (for solid component } s), \quad \ldots\ldots\ldots (A\text{-}2)$$

where V is the volume of the gridblock. The fully implicit scheme used here requires the derivatives of R_i and R_s with respect to the unknowns: specifically, pressure, saturation, mole fractions, and solid concentrations. Because the stoichiometric coefficients are constants, the derivatives for the reaction terms are given by

$$\frac{\partial R_i}{\partial p} = V\sum_{j=1}^{n_p}\sum_{k=1}^{n_k}\left(\nu'_{ij,k}-\nu_{ij,k}\right)\frac{\partial r_k}{\partial p}, \quad \ldots\ldots\ldots (A\text{-}3)$$

$$\frac{\partial R_i}{\partial S_\beta} = V\sum_{j=1}^{n_p}\sum_{k=1}^{n_k}\left(\nu'_{ij,k}-\nu_{ij,k}\right)\frac{\partial r_k}{\partial S_\beta}, \quad \ldots\ldots\ldots (A\text{-}4)$$

$$\frac{\partial R_i}{\partial X_{\alpha\beta}} = V\sum_{j=1}^{n_p}\sum_{k=1}^{n_k}\left(\nu'_{ij,k}-\nu_{ij,k}\right)\frac{\partial r_k}{\partial X_{\alpha\beta}}, \quad \ldots\ldots\ldots (A\text{-}5)$$

and

$$\frac{\partial R_s}{\partial C_\chi} = V\sum_{k=1}^{n_k}\left(\nu'_{s,k}-\nu_{s,k}\right)\frac{\partial r_k}{\partial C_\chi}, \quad \ldots\ldots\ldots (A\text{-}6)$$

where α is the fluid-component index, β is the fluid-phase index, and χ is the solid-component index. The concentrations of the fluid components are not directly computed. Instead, they are represented by pressure, saturation, and molar fractions. The chain rule is used to calculate the derivatives of r_k with respect to these unknowns. These derivatives are calculated as follows:

$$\frac{\partial r_k}{\partial p} = \sum_{j=1}^{n_p}\sum_{i=1}^{n_c}\frac{\partial r_k}{\partial C_{ij}}\frac{\partial C_{ij}}{\partial p}, \quad \ldots\ldots\ldots (A\text{-}7)$$

$$\frac{\partial r_k}{\partial S_\beta} = \sum_{j=1}^{n_p}\sum_{i=1}^{n_c}\frac{\partial r_k}{\partial C_{ij}}\frac{\partial C_{ij}}{\partial S_\beta}, \quad \ldots\ldots\ldots (A\text{-}8)$$

and

$$\frac{\partial r_k}{\partial X_{\alpha\beta}} = \sum_{j=1}^{n_p}\sum_{i=1}^{n_c}\frac{\partial r_k}{\partial C_{ij}}\frac{\partial C_{ij}}{\partial X_{\alpha\beta}}. \quad \ldots\ldots\ldots (A\text{-}9)$$

We also need expressions for the derivatives appearing on the right-hand sides of Eqs. A-7 through A-9. The derivatives of fluid concentration are given by

$$\frac{\partial C_{ij}}{\partial p} = \frac{\partial \rho_j}{\partial p}S_j\phi X_{ij} + \rho_j\frac{\partial \phi}{\partial p}S_j X_{ij}, \quad \ldots\ldots\ldots (A\text{-}10)$$

$$\frac{\partial C_{ij}}{\partial S_\beta} = \rho_j\delta_{j\beta}\phi X_{ij}, \quad \ldots\ldots\ldots (A\text{-}11)$$

and

$$\frac{\partial C_{ij}}{\partial X_{\alpha\beta}} = \frac{\partial \rho_j}{\partial X_{\alpha\beta}}S_j\phi X_{ij} + \rho_j\phi S_j\delta_{i\alpha}\delta_{j\beta}. \quad \ldots\ldots\ldots (A\text{-}12)$$

Assuming the elementary rate law holds, the derivative of the reaction rate with respect to fluid concentrations is

$$\frac{\partial r_k}{\partial C_{ij}} = \frac{\nu_{ij,k}r_k}{C_{ij}}. \quad \ldots\ldots\ldots (A\text{-}13)$$

Combining the expressions, the derivatives of the reaction term R_i with respect to the unknowns are

$$\frac{\partial R_i}{\partial p} = V\sum_{j=1}^{n_p}\sum_{k=1}^{n_k}\left(\nu'_{ij,k}-\nu_{ij,k}\right) \times\left[\sum_{j=1}^{n_p}\sum_{i=1}^{n_c}\frac{\nu_{ij,k}r_k}{C_{ij}}\left(\frac{\partial \rho_j}{\partial p}S_j\phi X_{ij} + \rho_j\frac{\partial \phi}{\partial p}S_j X_{ij}\right)\right], \quad \ldots\ldots (A\text{-}14)$$

$$\frac{\partial R_i}{\partial S_\beta} = V\sum_{j=1}^{n_p}\sum_{k=1}^{n_k}\left(\nu'_{ij,k}-\nu_{ij,k}\right)\times\left[\sum_{j=1}^{n_p}\sum_{i=1}^{n_c}\frac{\nu_{ij,k}r_k}{C_{ij}}\left(\rho_j\delta_{j\beta}\phi X_{ij}\right)\right], \quad \ldots\ldots\ldots (A\text{-}15)$$

and

$$\frac{\partial R_i}{\partial X_{\alpha\beta}} = V \sum_{j=1}^{n_p} \sum_{k=1}^{n_k} \left(\nu'_{ij,k} - \nu_{ij,k} \right) \times \left[\sum_{j=1}^{n_p} \sum_{i=1}^{n_c} \frac{\nu_{ij,k} r_k}{C_{ij}} \left(\frac{\partial \rho_j}{\partial X_{\alpha\beta}} S_j \phi X_{ij} + \rho_j \phi S_j \delta_{i\alpha} \delta_{j\beta} \right) \right]. \quad \text{(A-16)}$$

These equations provide the derivatives related to the kinetic reactions that are required in the Jacobian matrix.

Yaqing Fan is a PhD student in the Department of Energy Resources Engineering at Stanford University. He holds a BS degree from the University of Science and Technology of China in mechanical engineering and an MS degree from Stanford University in petroleum engineering. He is interested in coupled reaction and flow simulations with application to CO_2 sequestration and in-situ upgrading processes. He served as vice-president of the Stanford SPE Student Chapter from 2007 to 2008. **Louis J. Durlofsky** is the Otto N. Miller professor and chairman in the Department of Energy Resources Engineering at Stanford University. He was previously affiliated with Chevron Energy Technology Company. Durlofsky holds a BS degree from The Pennsylvania State University, as well as MS and PhD degrees from the Massachusetts Institute of Technology, all in chemical engineering. He codirects the Stanford University Industrial Affiliates Programs on Reservoir Simulation (SUPRI-B) and Advanced Wells (SUPRI-HW) and is also active in the Stanford Smart Fields Consortium. **Hamdi Tchelepi** is Associate Professor of Energy Resources Engineering at Stanford University. He holds a PhD degree in petroleum engineering from Stanford. He codirects the SUPRI-B and is interested in modeling unstable flows and in developing multiscale formulations and scalable solvers with application to reservoir flow simulation and subsurface CO_2 sequestration.